Kinetics of decomposition in ionic solids: neutron scattering study of the system AgBr-NaBr

Kinetics of decomposition in ionic solids: neutron scattering study of the system AgBr–NaBr

Götz Eckold

Institut für Physikalische Chemie der Universität Göttingen, Tammannstrasse 6,
D-37077 Göttingen, and Sonderforschungsbereich 345, Germany

Abstract
The kinetics of decomposition in the quasibinary ionic system AgBr–NaBr has been studied by time-resolved neutron diffraction and small-angle scattering. The temperature regimes for nucleation and for spinodal decomposition are clearly distinguished. The coherent critical point is estimated as 458 ± 5 K which is about 100 K below the maximum of the chemical binodal. Even at low temperatures the chemical demixing is completed within some 100 s resulting in a metastable state which is characterized by coherency strains and internal stresses of the order of 0.3 GPa. The mechanical relaxation of the lattice takes place on a much longer timescale after the correlation length of the decomposition pattern is increased to some critical value larger than 40 nm.

1. Introduction

The process of phase separation in the solid state is of great technical relevance not only for metallic systems in which precipitation hardening is frequently used to improve the performance of materials but also for soft matter like polymer blends which have become more and more important in recent times. Hence, the mechanism of decomposition and the formation of topological structures due to the precipitation of a second phase have been studied extensively in the past using both theoretical and experimental techniques [1–5]. The extent of a miscibility gap in a system with two or more components is directly related to the interaction between the constituents and can be described by thermodynamic quantities. More detailed information about system properties can, however, be obtained by investigating the kinetics of decomposition: the observation of transient states in a non-equilibrium system which is transforming from a homogeneous state into a two-phase state allows one to characterize trajectories and time evolution even on a microscopic scale.

Several mechanisms are usually distinguished depending on the preparation of the demixing system. Nucleation and growth processes are believed to dominate the phase separation after a quench into the metastable region of the miscibility gap. Here, the free energy can be reduced by concentration fluctuations of large amplitudes but small spatial extent. If, however, a homogeneous system is cooled into the thermodynamically unstable region below the spinodal, fluctuations of small amplitudes and large wavelengths become stable and are able

to grow as a function of time—a continuous process which is known as spinodal decomposition. In metallic alloy systems this mechanism has been rather controversial in the past and cluster models for the phase separation have been proposed [6].

While a huge number of investigations on metallic or polymer systems have been published, the kinetics of phase separation in ionic systems has hardly been studied at all. However, silver, copper or alkali halides with their rather large (cation) mobilities may be regarded as quite ideal model systems, since the anion sublattice provides an almost rigid frame for demixing processes which are almost completely confined to the cation subsystem. Some data exist for the systems AgCl–NaCl [7–10], NaCl–KCl [11–13] and NaBr–KBr [14]. The review of Jantzen and Herman [15] provides an overview with special emphasis on non-metallic systems. Moreover, first diffraction data on the AgBr–NaBr have been published in [16–18].

The morphology of the decomposing system is usually studied by experiments of two types. Direct observation by transmission electron microscopy, on the one hand, yields the time-dependent microstructure. This method is applicable at least to metallic systems if the sample under consideration can be quenched sufficiently quickly to room temperature, where diffusion processes are almost completely frozen. Small-angle (x-ray or neutron) scattering experiments, on the other hand, allow one to determine the pair correlation function and, hence, the mean size of the precipitates [19, 20]. Such investigations may be performed *in situ* during the actual decomposition process. For systems with sufficiently large differences between the lattice constants of the individual phases, diffraction data can provide additional and complementary information. Hence, the decomposition process can also be monitored by means of the time evolution of Bragg reflections or Debye–Scherrer rings (wide-angle scattering) [21].

In the present paper we report on experiments which combine small-angle neutron scattering (SANS) with time-resolved neutron diffraction in the quasibinary system AgBr–NaBr using a stroboscopic technique [21]. The silver–alkali halide systems provide a variety of different features which should influence the demixing process very substantially. First, from the structural point of view, most of the compounds exhibit the NaCl structure and quite simple phase diagrams with an almost symmetric miscibility gap. Even in more complicated systems, like CuBr–AgBr which yields several phases with different structures, the anion sublattice is nearly preserved and it is the ordering of the cations which determines the structural properties [22]. Second, the mobilities of different cations cover a broad range, yielding different kinetic behaviours. In the AgBr–NaBr system the diffusivity of Ag^+ is about one order of magnitude larger than that of Na^+, while Br^- is much less mobile [23]. Third, the lattice parameters of the pure substances vary appreciably, offering the possibility to tune the effect of internal strains which, in turn, influences the spinodal and, hence, the mechanism of decomposition.

As the first of a series, the system AgBr–NaBr has been chosen for the present study. Neither of the pure substances exhibit any solid-state phase transition. The lattice constants of NaBr and AgBr differ by more than 3%. Hence, the splitting of the Bragg reflections during demixing can be resolved rather easily. Interestingly, NaBr exhibits the larger lattice constant (0.5971 nm for ambient temperature as compared to 0.5774 nm for AgBr [24, 25]), although the ionic radius of sodium is smaller than that of silver. This effect seems to be a direct consequence of the large polarizability of silver ions [26] which is also reflected by the strong anharmonicity of the AgBr lattice [27, 28]. Due to the difference in lattice constant, the mixed system $Ag_x Na_{1-x} Br$ exhibits a pronounced miscibility gap, as shown in figure 1, which is almost symmetrical, with a critical temperature of $T_c \approx 558$ K and a critical concentration of $x_c \approx 0.506$ as reported in the literature [24, 25, 29–31]. (Note that throughout this paper, concentrations are always given in mole fractions of AgBr.)
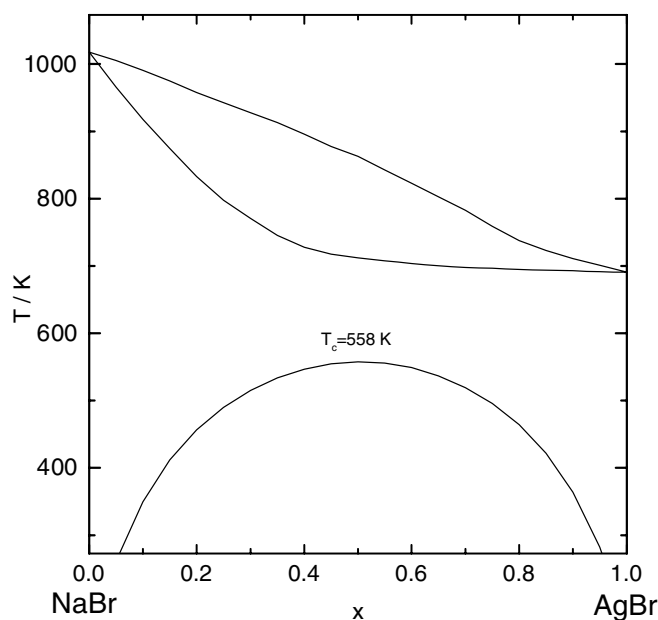
Figure 1. The phase diagram of the system AgBr–NaBr, after [24, 25, 30, 31].

The kinetics of decomposition in $Ag_xNa_{1-x}Br$ has been studied previously by macroscopic methods like calorimetry [31] and transport experiments [32]. The first microscopic experiments were performed by Trzeciok and Nölting [24, 25] using x-ray diffraction. The quality of the data obtained, however, precluded a quantitative interpretation. The first time-resolved neutron diffraction data were published by Eckold and co-workers [16–18], along with a simple phenomenological model for the evolution of the phase separation [17]. This model is based on the assumption that the profiles of Bragg reflections can be directly translated into a distribution of concentrations via Végard's rule, and the influence of internal strains is neglected.

The present investigation provides new detailed information as regards the underlying mechanism, by combining diffraction and small-angle neutron scattering. We concentrate on almost critical compositions and will show that internal strains and residual stresses, in fact, lead to metastable states which can be observed over a long time interval. It is our aim to demonstrate that this ionic system is an almost ideal system in which to study the transition from the nucleation regime at higher temperatures to the fluctuation regime at lower temperatures.

The paper is organized as follows. In the second section, details of the neutron scattering experiments are given. The results of diffraction and small-angle experiments in the high-temperature range and the qualitatively different behaviour at lower temperatures will be presented and discussed in the subsequent sections. A summarizing discussion of the mechanism of decomposition is the subject of section 4 which is followed by brief conclusions.

2. Experimental procedure

For the present investigations, polycrystalline samples were used. After having ground and graded the pure components (AgBr Merck 99%, NaBr Merck Suprapur 99%), mixtures with almost critical concentration were prepared and pressed into pellets of 40 (20) mm diameter and

about 4 (2) mm thickness for the diffraction (small-angle scattering) experiments. Wrapped in silver foil, these samples were mounted in a furnace using an aluminium can which provided a good temperature homogeneity. The temperature was determined with an overall accuracy of about 2 K by several Ni–NiCr thermocouples close to the sample. Two types of experiment were performed using different furnaces: a standard furnace provides an inert gas atmosphere (helium) but restricts the cooling rate to less than 0.25 K s^{-1}. Hence, this furnace could be used for temperatures larger than about 440 K which is approximately 120 K below the critical temperature. A special heating device with low heat capacity was used to reach lower ageing temperatures. Here, the samples were cooled in air and a fan was used during the quench in order to achieve a rate of up to 4 K s^{-1}. In this way, quenches down to 320 K could be realized.

The homogenization of the sample was achieved by annealing at temperatures well above T_c. This process was monitored by observing either Bragg reflections or the small-angle integrated intensity.

Neutron diffraction experiments (wide-angle scattering) were performed using the triple-axis spectrometer UNIDAS at the FRJ-2 reactor in Jülich. The wavelength was chosen to be 0.236 nm and the overall collimation was tightened to $0.25°$. For the kinetic experiments, during the phase separation the technique of time-resolved triple-axis spectroscopy was used, the details of which have been described elsewhere [21]. For every setting of the spectrometer, the sample temperature was varied periodically between 590 K (well above T_c) and several decomposition temperatures T_d in the range from 360 K to 520 K. The scattered neutrons were detected as a function of time with respect to the beginning of the temperature cycle. Repeating this procedure for different momentum transfers allows one to determine the time dependence of the Bragg profiles. The period of the cycles was adapted to the temperature-dependent kinetics of the decomposition process. In general, neutrons were collected in time channels of width 30 s during phase decomposition and 5 s during quenching and heating.

For the small-angle scattering experiments, the two instruments V4 at the BERII reactor in Berlin and KWS1 at the FRJ-2 were used. Wavelengths between 0.46 and 0.70 nm and detector positions between 4 m and 12 m allowed coverage of a Q-range from 0.045 nm^{-1} to 7 nm^{-1}. The wavelength resolution was about 10%. Data were taken sequentially after quenching to the ageing temperature and, hence, the time resolution is directly related to the counting statistics. The smallest time step between two subsequent data sets was 60 s. The data acquisition system for kinetic experiments at KWS1 guaranteed that there was no dead time between adjacent spectra. The data were corrected in the usual way for detector efficiency, background and self-shielding and the radial average was taken. The thickness of the sample was adjusted to ensure that the scattering probability was less than 10%. Hence, multiple-scattering effects are avoided. Using water or lupolen samples, we were able to obtain absolute values of the scattered intensity.

3. Results

3.1. Decomposition at high temperatures (the nucleation regime)

3.1.1. Diffraction.   In figure 2 the time evolution of the (200) Bragg reflection is displayed for two overall concentrations, $Ag_{0.41}Na_{0.59}Br$ and $Ag_{0.50}Na_{0.50}Br$, at different decomposition temperatures. In these 3D plots, the x- and y-axes correspond to the wave-vector transfer Q in units of $2\pi/a_{nom}$ ($a_{nom} = 0.595$ nm) and to the time in seconds, respectively. The intensity is plotted along the z-axis. For convenience, the zero point of the timescale ($t = 0$) is chosen as the moment when the ageing temperature is actually reached. At the beginning
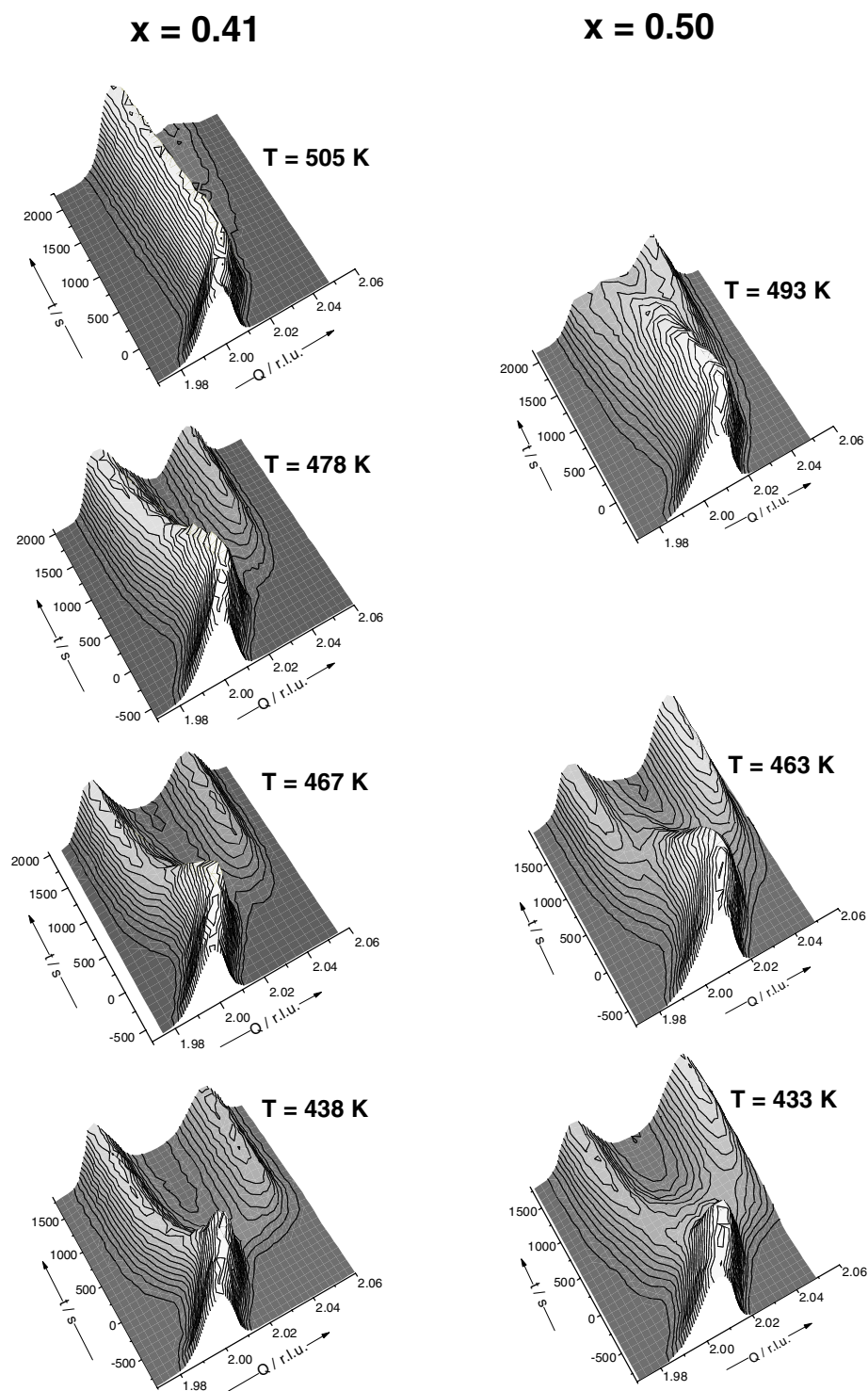
x = 0.41

x = 0.50

Figure 2. Time evolution of the (200) Bragg reflection of $Ag_x Na_{1-x} Br$ for two compositions (left: $x = 0.41$; right: $x = 0.50$) at different temperatures.

of the temperature cycle ($t < 0$), the sample is in the homogeneous state at about 590 K and the reflection is represented by a well defined Gaussian. During the cooling phase, the peak position shifts to larger wave vectors corresponding to the thermal contraction of the lattice. From the peak shift and temperature shift, the coefficient of thermal expansion is determined to be $5.6 \times 10^{-5}\,\mathrm{K}^{-1}$ in very good agreement with data from the literature [24] which were obtained under equilibrium conditions. This finding along with the fact that there is no broadening of the Bragg reflection during cooling indicates a good temperature homogeneity across the sample.

For $t > 0$, a splitting of the Bragg peak is observed which is more pronounced at lower temperatures. This splitting directly reflects the phase separation where components at larger Q, i.e. smaller lattice constants, correspond to silver-rich phases and components at smaller Q correspond to sodium-rich phases. Obviously, the decomposition is strongly accelerated at lower temperatures, whereas at 505 K the peak splitting in the time range under consideration can hardly be seen in the 3D representation of figure 2. At lower temperatures, however, the evolution of the Bragg profile from a single peak in the initial state via a structure with three or more components in the early stages towards the two well defined peaks at large times corresponding to the stable equilibrium concentrations is clearly visible.

After half of the cycling period, the temperature is increased again and the homogenization of the sample takes place on a much shorter timescale and is completed within about 300 s, which is not shown in figure 2. Hence, at the beginning of the next temperature cycle, the sample is definitely in the initial state and passes through identical states in each cycle. It should be noted that the results are perfectly reproducible. In particular, there are no indications for slow variations of sample properties, such as grain structure and grain size, during periodic demixing and homogenization.

More quantitatively, the data can be analysed if the individual spectra at constant time t are considered. As an example, figure 3 displays two spectra obtained for an overall concentration of $x = 0.41$ and the decomposition temperature $T_d = 467$ K at $t = 415$ s and $t = 865$ s. The spectra can be fitted to three Gaussians which may be attributed to three rather well defined phases with different lattice constants:

(1) The central component with the intensity I_m and peak position Q_m or lattice constant a_m corresponds to a mixed phase.
(2) The component at smaller wave vectors Q_{Na} corresponds to the sodium-rich phase with a larger lattice constant a_{Na} and the intensity I_{Na}.
(3) The component at larger wave vectors Q_{Ag} corresponds to the silver-rich phase with a smaller lattice constant a_{Ag} and the intensity I_{Ag}.

The concentration (mole fraction) and the total number of moles for the individual phases are denoted by x_m, N_m, x_{Na}, N_{Na}, x_{Ag}, N_{Ag}, respectively.

As a typical example, figure 4 displays the time dependence of the (integrated) intensities and peak positions of the three components for the same overall composition as for figure 3. It can readily be seen that the lattice parameters of the product phases are almost time independent. This behaviour is characteristic for a nucleation mechanism of decomposition.

Even if there was a considerable correlation between the fit parameters, the linewidth for the mixed parent phase turned out to be almost time independent. Hence, in order to reduce the statistical error, it was fixed to the width obtained in the homogeneous phase (0.014 r.l.u. $\approx 0.15\,\mathrm{nm}^{-1}$) which is essentially determined by the experimental resolution. In contrast, the Bragg peaks of the product phases are somewhat broader ($\approx 0.2\,\mathrm{nm}^{-1}$) in the early stages of decomposition and become narrow at later times. In principle, this behaviour might be due either to grain size effects, to concentration gradients or to internal strains. If the observed broadening were attributed to the size of the precipitates, characteristic diameters of
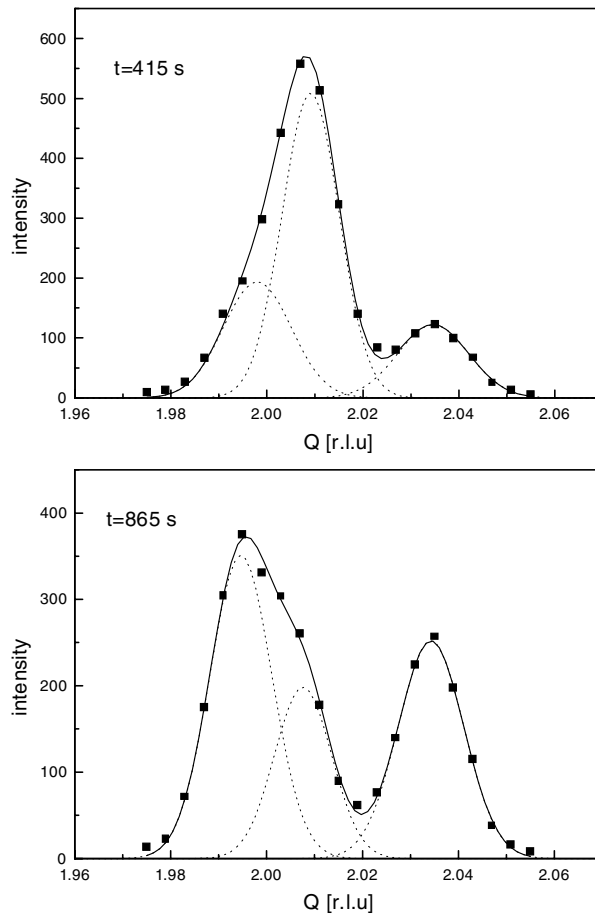
Figure 3. Bragg profiles of $Ag_{0.41}Na_{0.59}Br$ at different ageing times and $T = 467$ K.

50 nm would result at small t. Those dimensions are, however, incompatible with the results of the small-angle scattering experiments (see section 3.1.2), which provide evidence for the existence of significantly larger grains. Moreover, large concentration gradients are unlikely to exist since the average lattice parameters of the product phases hardly change during the decomposition. Hence, the broadening of the Bragg reflections is most probably the result of internal strains.

From the integrated intensities of the three individual components, one may derive a degree of decomposition α defined as the volume fraction

$$\alpha = \frac{N_{Ag} + N_{Na}}{N_{Ag} + N_{Na} + N_m} \tag{1}$$
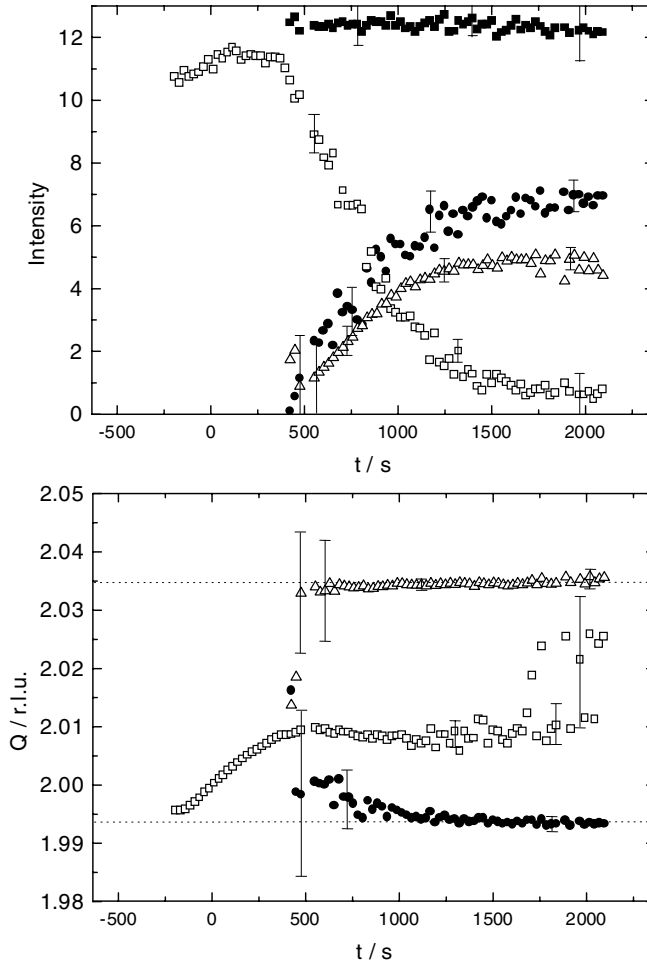
where the amounts of the different phases are related to the scattered intensities and to the (concentration-dependent) scattering lengths b_i via the proportionality

$$N_i \propto I_i/(b_i)^2. \tag{2}$$

The scattering lengths are calculated from the mole fractions x_i of the respective phases according to

$$b_i = x_i b_{Ag} + (1 - x_i)b_{Na} + b_{Br} \tag{3}$$

Figure 4. Time dependences of the intensities (upper part) and positions (lower part) for the three components of the Bragg reflection for $Ag_{0.41}Na_{0.59}Br$ at 467 K: $\square$: mixed phase; $\bullet$: sodium-rich phase; $\triangle$: silver-rich phase; $\blacksquare$: total Bragg intensity.

($b_{Ag} = 0.597 \times 10^{-12}$ cm, $b_{Na} = 0.363 \times 10^{-12}$ cm, $b_{Br} = 0.679 \times 10^{-12}$ cm). Hence, they vary from $b_{NaBr} = 1.042 \times 10^{-12}$ cm to $b_{AgBr} = 1.276 \times 10^{-12}$ cm.

The mole fractions, in turn, are estimated from the peak positions or the lattice constants using Végard's rule as a rough estimate. At least in equilibrium outside the miscibility gap, the validity of Végard's rule has been confirmed by Tsuji et al [29].

Thus, we obtain the time dependence of the degree of decomposition as shown in figure 5. The data provide a 'lump' description of the demixing process without taking into account any structural changes such as the relaxation of strains. The profiles $\alpha(t)$ resemble stretched exponential functions of the type which are frequently used to describe nucleation and growth processes [33, 34]. The time constants are of the order of 1000 s and increase appreciably with temperature. This finding is compatible with results of conductivity experiments performed by Preidel and Nölting [32]. Obviously, there is a strong acceleration of the demixing process at lower temperatures due to the increased thermodynamic driving force and, hence, to the increased nucleation rate.
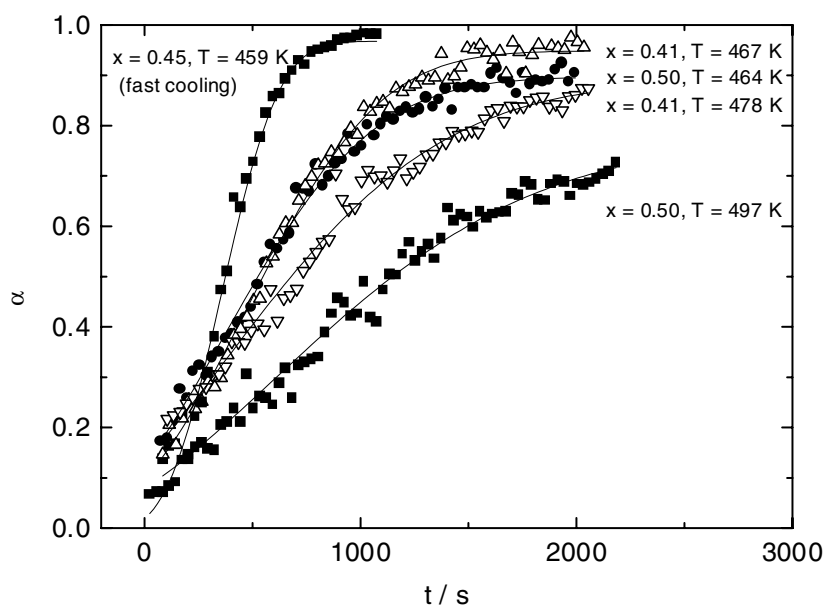
Figure 5. Time dependences of the degree of decomposition α for different temperatures and overall compositions $Ag_x Na_{1-x} Br$ (the lines are fits using a stretched exponential function).

Furthermore, we infer from figure 5 that the kinetic behaviour is almost unchanged if the overall concentration is varied from $x = 0.50$ to $x = 0.41$.

Note that the cooling rate of 0.25 K s^{-1} in these experiments is not sufficient to suppress demixing during cooling. Rather, on reaching 497 K (464 K), 10% (20%) of the sample is already decomposed. Moreover, these intermediate precipitates formed at higher temperatures decelerate the demixing process at the final ageing temperature. This can be directly seen by comparison with the results from fast-quench experiments (4 K s^{-1}) which are also included in figure 5. Under these conditions no significant decomposition is observed during cooling and the subsequent isothermal demixing process is clearly characterized by an appreciably smaller time constant of about 400 s. This finding may be regarded as a direct consequence of the enhanced rate for homogeneous nucleation with smaller critical grain size at lower temperatures. Intermediate precipitates built up during slow cooling hinder the complete phase separation since their growth and change in composition are restricted due to the reduced diffusion coefficient. (Note that the formal activation energy for diffusion was determined by Preidel and Nölting [32] to be about 90 kJ mol^{-1}.)

Carmesin *et al* [35] have investigated the influence of finite quench rates on the demixing process in some detail. They focused their attention on the spinodal regime and demonstrated that the long-wavelength fluctuations appearing during cooling influence the decomposition process very substantially at lower temperatures and lead, in fact, to a slowing down as soon as the activation energy is large enough.

Moreover, it is recognized that the lattice parameters of the product phases obtained after rapid cooling are in good agreement with the phase diagram as shown in figure 1 if Végard's rule is applied. Cooling at a rate of 0.25 K s^{-1}, however, leads to a silver-rich phase which exhibits a significantly (0.9 pm) larger lattice parameter. While in a previous interpretation [17] of preliminary data this effect was attributed to slightly different binodal concentrations, we now believe that it is a consequence of residual strains within the sample.

At temperatures well below 450 K the shape of the Bragg profiles changes drastically and the interpretation in terms of three well defined components fails. Instead, a continuous intensity distribution over a large Q-range is observed. For the detailed investigation of these phenomena, experiments with larger cooling rates have been performed which are described in section 3.2.

3.1.2. Small-angle scattering. The small-angle neutron scattering data for the high-temperature regime above 460 K exhibit a simple monotonic decrease of the scattered intensity with Q as shown in figure 6. Here, the scattering of the homogeneous phase is subtracted and, hence, the data directly represent the additional intensity due to decomposition. The data at large Q can be quantitatively described by Porod's Q^{-4}-law:

$$\frac{\mathrm{d}\Sigma}{\mathrm{d}\Omega}(Q) = 6\pi N \frac{V}{V_{\mathrm{tot}}}(\Delta\rho)^2 \frac{1}{R}\frac{1}{Q^4} = 6\pi\alpha(\Delta\rho)^2 \frac{1}{R}\frac{1}{Q^4} \tag{4}$$

where V_{tot} and V are the total volume of the sample and the volume of a single precipitate with radius R, respectively. N is the total number of precipitates and $\Delta\rho$ is the scattering contrast between precipitate and matrix. Note that the deviations of the experimental data from the Porod behaviour below $Q \approx 0.08$ nm^{-1} are due to resolution effects which lead to an increase of the scattered intensity.

Scattering of the Porod type is expected for a simple nucleation mechanism, yielding well defined grains of the product phases. The time dependence of the small-angle intensity integrated over the accessible Q-range (the Porod regime) is displayed in the inset of figure 6 and provides independent information about the size of the precipitates: if we neglect the change of particle density during decomposition, the product NV/V_{tot} is just the degree of decomposition α and, hence, the SANS intensity should be proportional to α/R. As shown in figure 7, there is a remarkable agreement between the SANS and the diffraction data: for slow cooling as well as for rapid cooling, the time evolution of the SANS intensity is almost identical to the corresponding behaviour of α. Consequently, there is no indication of a pronounced grain growth at the ageing temperature which would lead to a decrease of the SANS intensity in the Porod regime.

Equation (4) can be used to derive a rough estimate of the average radius of the precipitates from the asymptotic value at large t: neglecting the difference of the particle densities, we find for the scattering contrast

$$\Delta\rho = n\frac{b_{\mathrm{Ag}} - b_{\mathrm{Na}}}{2}\Delta x \tag{5}$$

where Δx is the width of the miscibility gap and n the particle density.

Using $n = 2 \times 10^{22}$ cm^{-3} and $\Delta x \approx 0.58$ for 473 K, we obtain a value for the average grain radius of about 230 nm.

Both techniques, diffraction as well as SANS, give strong evidence that for temperatures above $\approx$455 K the decomposition in Ag$_{1-x}$Na$_x$Br is dominated by a nucleation mechanism. Below, not only do the diffraction data exhibit a qualitatively different behaviour, but also the small-angle scattering shows pronounced deviations from Porod's law in the early stages of the decomposition.

## 3.2. Decomposition at low temperatures (the fluctuation regime)

3.2.1. Diffraction. The experiments with larger quench rates allow us to investigate the decomposition process at temperatures down to 365 K. Figure 8 displays the diffraction data for an overall concentration of $x = 0.45$. At $T = 459$ K, which is still in the nucleation regime, three
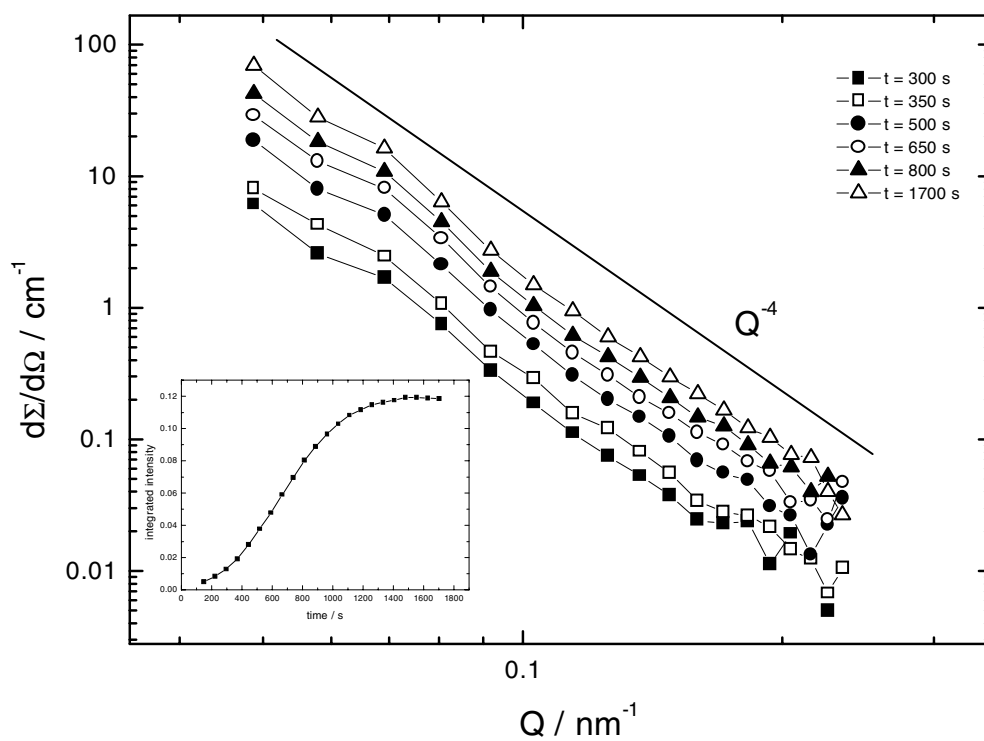
Figure 6. The small-angle scattering intensity of $Ag_{0.5}Na_{0.5}Br$ during the decomposition at 473 K. The time dependence of the intensity integrated over the accessible Q-range is shown in the inset.
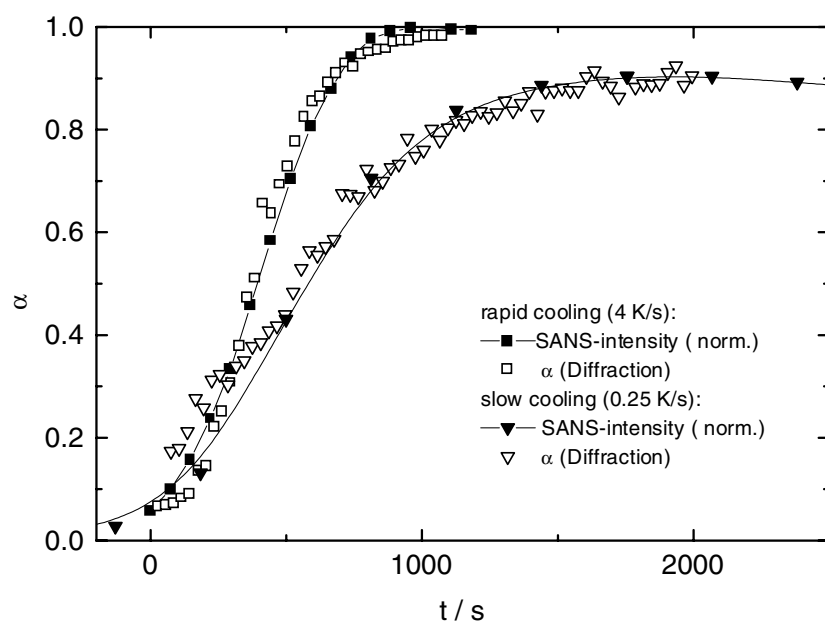
Figure 7. The time dependence of the SANS intensity and the degree of decomposition at 473 K for slow and rapid cooling.
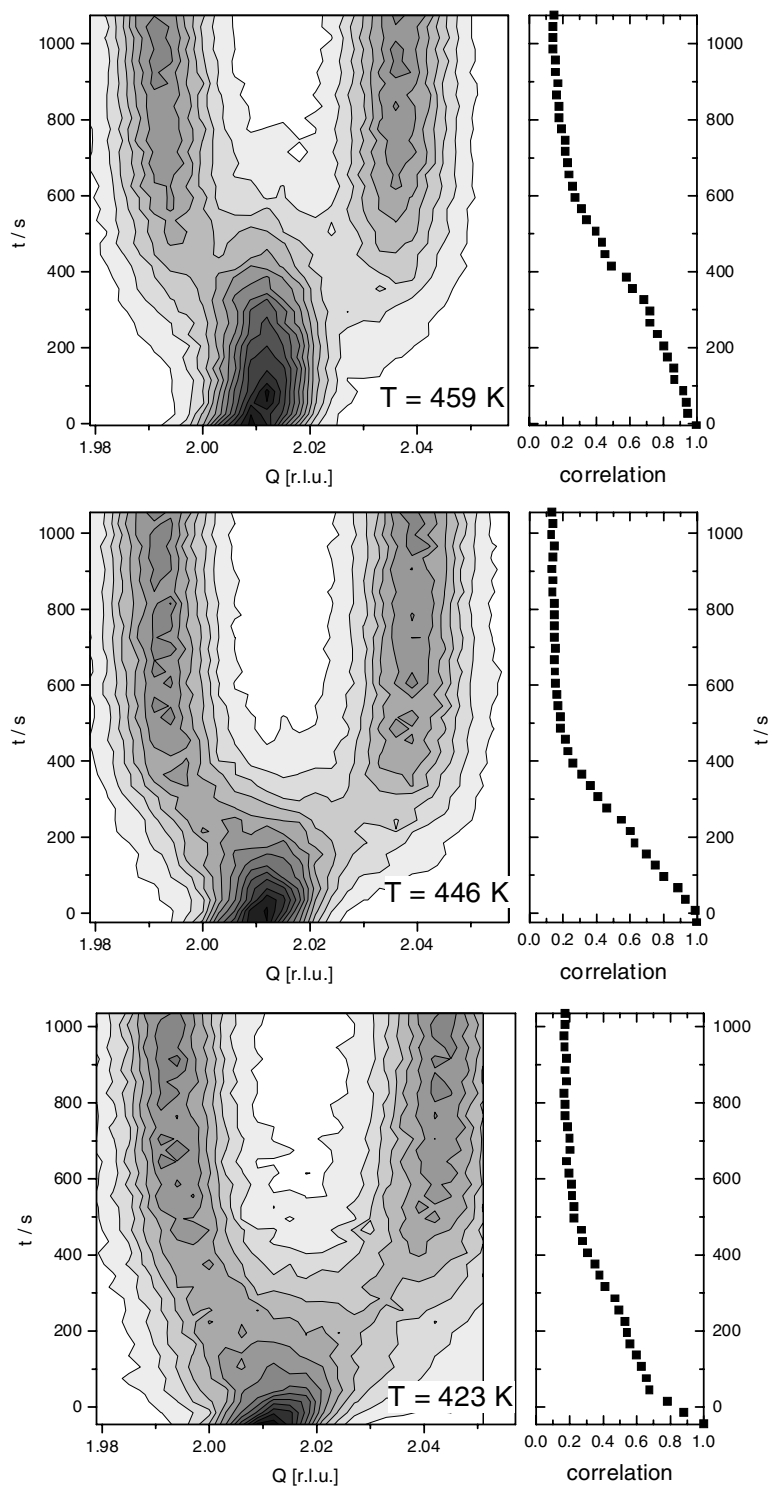
Figure 8. Time evolution of the (200) Bragg reflection of $Ag_{0.45}Na_{0.55}Br$ at low temperatures.
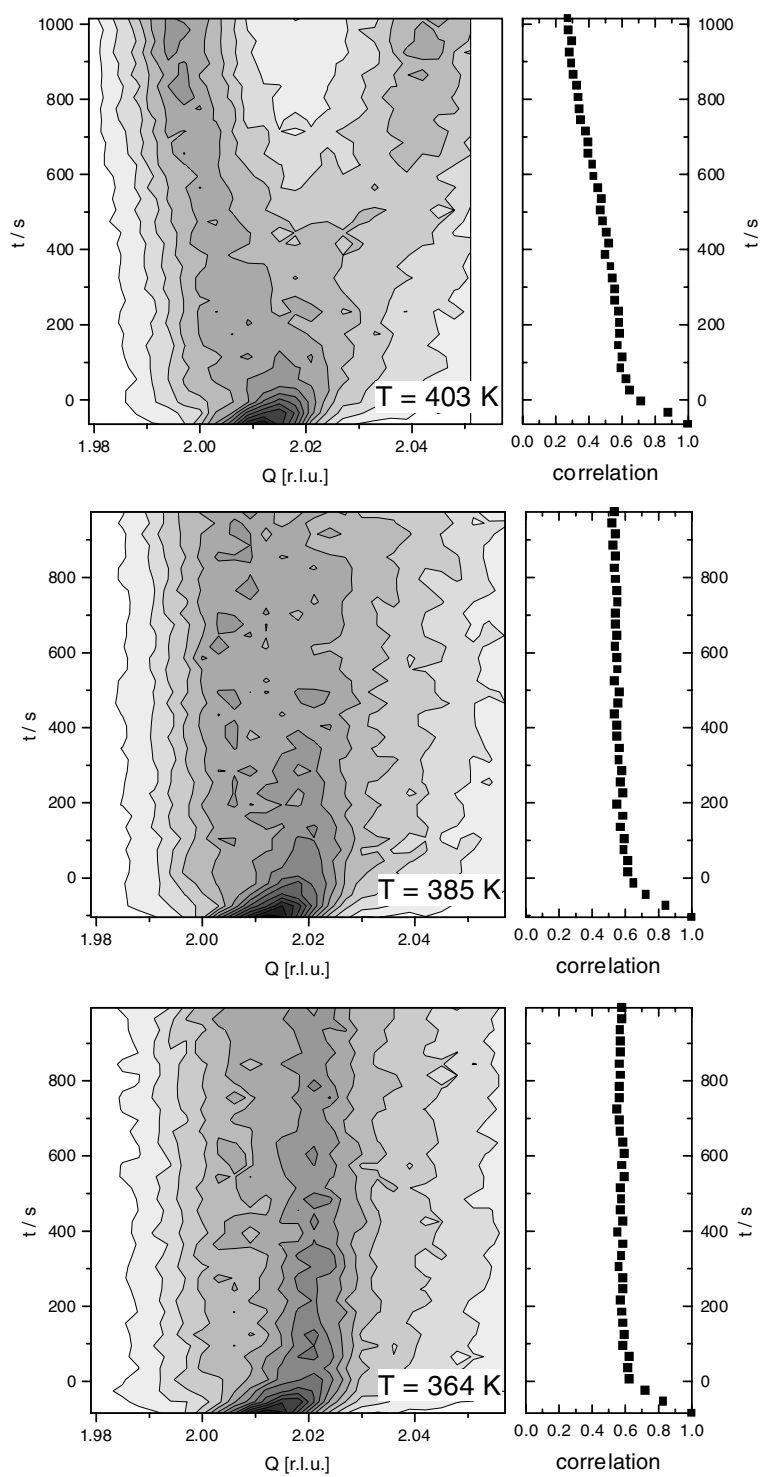
Figure 8. (Continued)

rather well defined components of the Bragg peak can be distinguished. Below about 440 K, however, a completely different behaviour is clearly observed: when the ageing temperature is reached, the Bragg reflection is broadened almost instantaneously. While at 423 K and 403 K the formation of the equilibrium phases is clearly observed within the timescale of the present experiment, the continuous intensity distribution remains nearly unchanged at lower temperatures. Obviously, there is no well defined crystal lattice at 385 K even after an ageing time of 1000 s.

It should be noted that the broadening is not due to processes occurring during cooling. Rather, immediately after the quench the parent phase exhibits a well defined Bragg peak at just the position which is expected from the coefficient of thermal expansion. Hence, thermal gradients can be neglected.

Careful inspection of figure 8 shows that the broadening takes place within the first 50–100 s after the ageing temperature has been reached. Hence, the structure with a well defined lattice constant is destroyed rather quickly on a timescale much shorter than that for the formation of the equilibrium phases.

It is obvious even from the contour plots in figure 8 that a quantitative description in terms of Gaussians is no longer possible at low temperatures. Instead, we use another approach for a more quantitative representation of the data: we introduce a time-dependent intensity correlation function or overlap integral:

$$C(t) = \left(\int I(Q, t) I(Q, t_0) \, dQ \right) \Big/ \left(\int [I(Q, t_0)]^2 \, dQ \right). \tag{6}$$

Here, $I(Q, t)$ is the scattered intensity at scattering vector Q and time t. $I(Q, t_0)$ represents a reference data set taken at the time t_0 when a single well defined Bragg peak is observed, which corresponds to the supercooled homogeneous phase. This correlation function $C(t)$ is thus a quantitative measure of the probability of finding an unchanged lattice parameter and characterizes the mechanical relaxation of the lattice during decomposition. The corresponding data are included in figure 8, and figure 9 allows a direct comparison of the behaviour at different temperatures. It should be noted that at long times, $C(t)$ actually does not decrease to zero even if the decomposition is complete. Due to resolution effects there is always an overlap between the two Bragg reflections of the decomposed phases and the initial Bragg peak of the parent phase. Hence, the asymptotic value $C(t \to \infty)$ depends on the width of the miscibility gap and decreases somewhat at lower temperatures. At temperatures above 440 K, the shape of $C(t)$ resembles a sigmoidal curve (see the upper part of figure 9). This is the regime where the spectra consist of rather well defined individual components. Below 440 K (see the lower part of figure 9), however, $C(t)$ exhibits a sharp step from 1 to about 0.6 within the first 100 s. Subsequently, a plateau is observed which becomes more pronounced at lower temperatures. At 403 K, this plateau extends over a time range of about 200 s, while at 385 K it is observed even up to the end of the period at about 1000 s. At very long times, $C(t)$ finally decreases slowly to its asymptotic value.

3.2.2. Small-angle scattering. Corresponding data for the small-angle regime are shown in figure 10 for 323 K and 373 K. Again, the scattering in the homogeneous phase is subtracted. The scattering is dominated by a correlation peak at wave-vector transfers Q_{max} of the order of 0.2–0.3 nm^{-1}. There is some parasitic scattering at very low Q which is almost independent of time and temperature and could be due to slightly different container scattering at high and low temperatures which is not eliminated by taking the difference spectra.

As a function of time, the correlation peak shifts to smaller Q corresponding to a coarsening of the decomposition pattern. This behaviour is characteristic for spinodal decomposition in
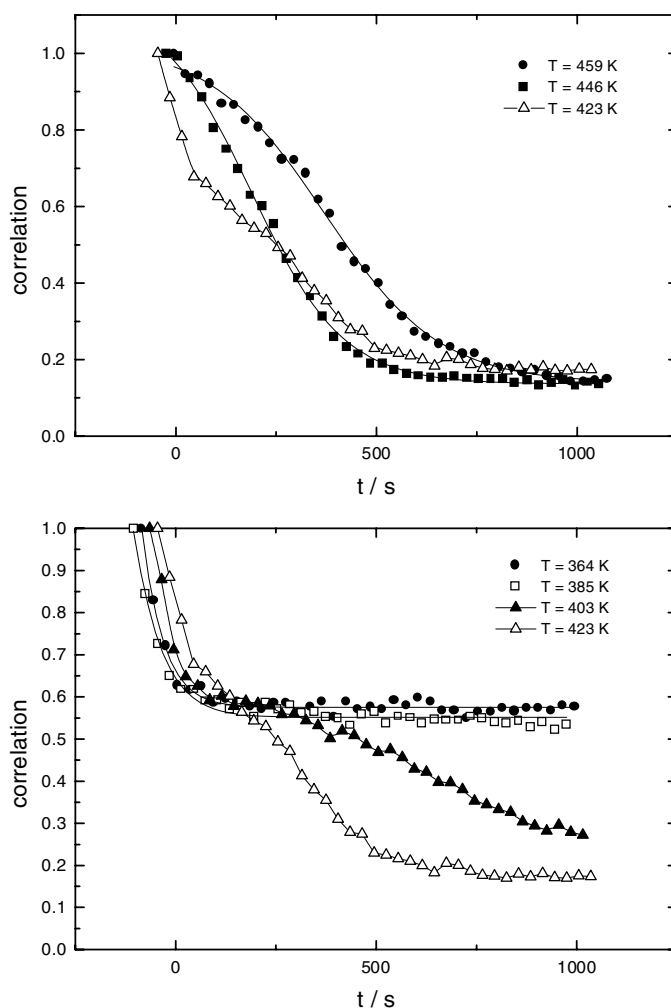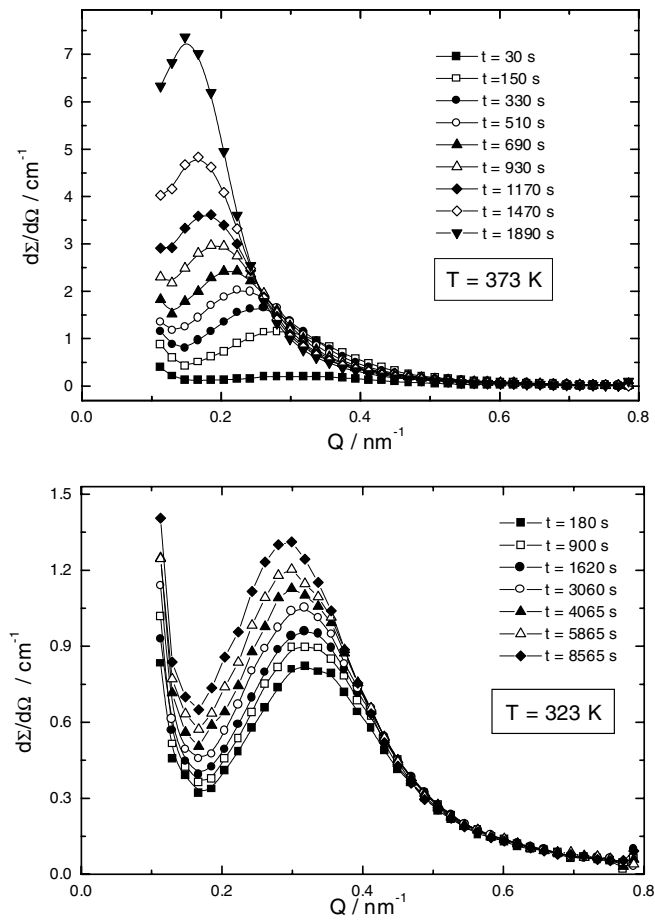
Figure 9. The time dependence of the correlation function for $Ag_{0.45}Na_{0.55}Br$ at various temperatures.

non-linear systems. Hence, it is obvious that the linear Cahn–Hilliard [36] and the linearized Cahn–Hilliard–Cook model [37] for spinodal decomposition which predict the growth of concentration fluctuations with a favoured wavelength are not applicable. Moreover, at 373 K we even observe the so-called crossing of the tails at short times—another characteristic feature of non-linear behaviour.

The time dependence of Q_{max} is presented in figure 11. There is an initial time regime where Q_{max} is only slightly time dependent. It extends to some 100 s at 373 K and to almost 1000 s at 323 K. The corresponding initial correlation lengths $2\pi/Q_{max}$ decrease somewhat with temperature from 20 nm at 373 K to 19 nm at 323 K. The subsequent coarsening process is more pronounced at higher temperatures. At 373 K, in particular, the limiting $t^{-1/3}$-law of Lifshitz and Slyozov [38] is well established already after 300 s, while at 323 K even after several 1000 s the correlation peak is shifted by only a few 0.01 nm^{-1}. After ageing for 1600 s at 373 K the correlation length is increased from 20 nm to about 40 nm.

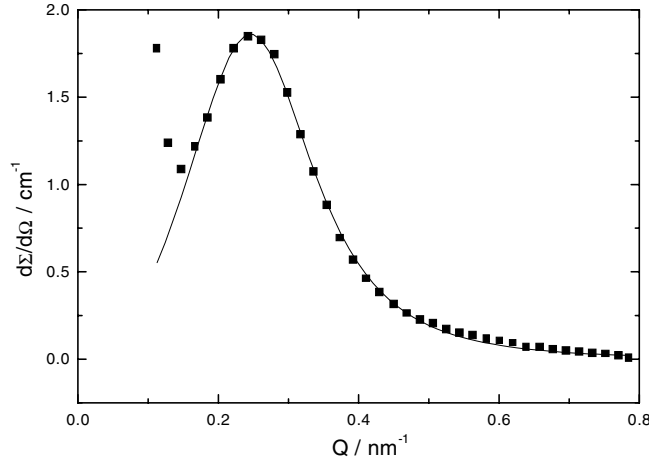**Figure 10.** Time evolution of the small-angle intensity at 373 K (top) and at 323 K (bottom).
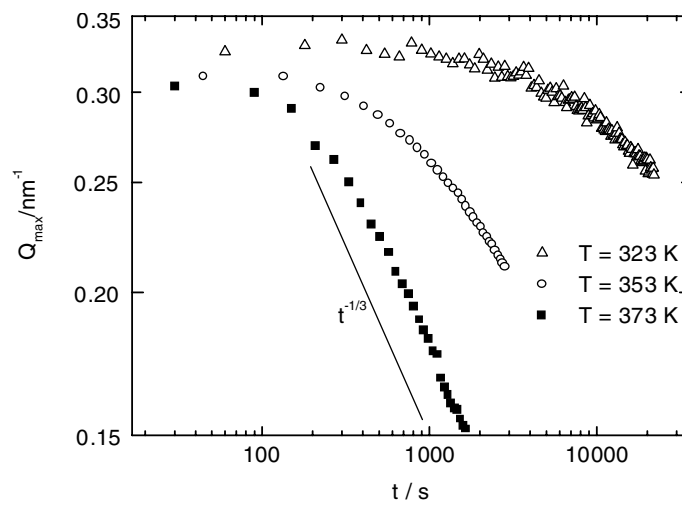
Figure 11. The time dependence of the position Q_{max} of maximum small-angle intensity.

At very long times, when approaching equilibrium, the correlation peak disappears and merges into a Porod Q^{-4}-tail.

The experimental data can be quantitatively described by the phenomenological *ansatz* of Furukawa [39, 40]:

$$\frac{d\Sigma}{d\Omega}(Q) = A\left(1 + \frac{\beta}{\gamma}\right)\frac{(Q/Q_{max})^{\gamma}}{\beta/\gamma + (Q/Q_{max})^{\beta+\gamma}} \tag{7}$$

as shown in figure 12. Here, the exponents β and γ characterize the asymptotic behaviour of $d\Sigma/d\Omega$ at large Q ($d\Sigma/d\Omega \propto Q^{-\beta}$) and at small Q ($d\Sigma/d\Omega \propto Q^{\gamma}$), respectively. The fits of our present data yield values close to $\beta \approx 4.5$ and $\gamma \approx 2$.


Figure 12. A typical small-angle intensity profile taken at 353 K and 1485 s. The line is a fit to the Furukawa function.

The evolution of the integrated SANS intensity directly reflects the kinetics of the decomposition process. In order to obtain reliable intensities, a reasonable extrapolation of the experimental data to larger Q-values is crucial. We use the Furukawa function (7) for a fit of the small-angle profiles $Q^2 \, d\Sigma/d\Omega$ and calculate the integrated intensity according to

$$4\pi \int_0^{\infty} \frac{d\Sigma}{d\Omega}(Q)Q^2 \, dQ$$
$$= 4\pi A\left(1 + \frac{\beta}{\gamma}\right)\Gamma\left(\frac{\beta-3}{\beta+\gamma}\right)\Gamma\left(\frac{\beta+2\gamma+3}{\beta+\gamma}\right)\Big/\left[(\gamma+3)\left(\frac{\beta}{\gamma}\right)^{(\beta-3)/(\beta+\gamma)}\right]. \tag{8}$$

The corresponding results are shown in figure 13. Obviously, there is an initial phase of rapid demixing when the intensity jumps within some 100 s from zero to some 5×10^{20} cm^{-4}. At 323 K, it then keeps almost constant up to very long times. The data for $T = 373$ K, however, reveal that the initial phase is followed by a period of slow relaxation in which the intensity is continuously increasing. This behaviour is very different from the findings for metallic alloys like Al–Zn [41], e.g., where an almost linear increase of the intensity was observed over a very long period of time.

Scaling theories are frequently used to represent the evolution of decomposition structures [42–45]. If, in the later stages, the chemical decomposition is complete and the remaining demixing process is dominated by coarsening effects, it is expected that the scaled representation of the scattering cross section, namely $Q_{max}^3 \, d\Sigma/(d\Omega)(Q/Q_{max})$ for 3D systems, yields a time-independent universal function. Note that a scaling behaviour of this type requires
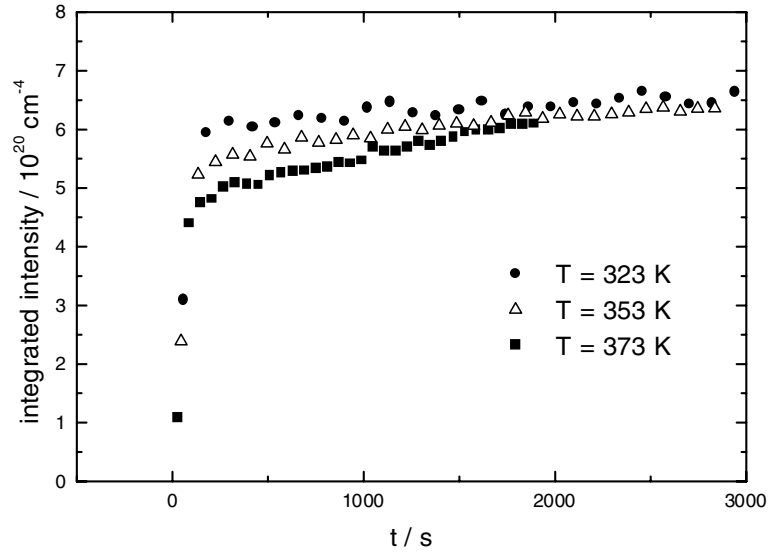
**Figure 13.** The time dependence of the integrated small-angle intensity for three different temperatures.

the integrated intensity to be constant. The corresponding experimental data are shown in figure 14 for two different temperatures. It can easily be seen that the scaling behaviour is rather well followed at $T = 323$ K over a large time interval from 600 to 8640 s, while at $T = 373$ K the scaled intensity is continuously increasing even after 1000 s. Inspection of the data yields, however, that at the latter temperature there is an intermediate time regime between about 600 s and 1400 s where the scaling law holds approximately, which is consistent with the evolution of the integrated intensity (figure 13). It is just in that time interval that the diffraction experiments exhibit broad Bragg reflections and the corresponding correlation function shows the plateau in figure 9.

Obviously, there are rather well defined stages of decomposition which seem to be governed by different mechanisms. Hence, we made no attempt to describe our data in terms of the non-linear models of Cook [37], Langer [46] or Langer, Bar-On and Miller [47].

In order to estimate the critical temperature of the coherent spinodal, T_s, which separates the metastable part of the miscibility gap from the unstable part and, hence, the regimes of the nucleation and fluctuation mechanisms, we proceed as follows: for different temperatures, we compare the small-angle intensity profiles corresponding to the first time step after quenching. These data are collected in figure 15. The double logarithmic scale allows one to distinguish quite easily between the Porod behaviour at high temperatures and the beginning of the formation of a correlation peak below T_s. It is obvious that the first indication of collective concentration fluctuations appears at 453 K, while at 463 K the SANS intensity decreases monotonically according to Q^{-4}. Hence, we conclude that the critical spinodal temperature is $T_s = 458 \pm 5$ K, about 100 K below the critical temperature T_c of the incoherent binodal.

This suppression ΔT_s of the spinodal is due to the coherency strains which appear if the (equilibrium) phases exhibit different lattice parameters. In the simplest approximation according to Cahn [48] (isotropic medium), ΔT_s can be calculated from

$$\Delta T = T_c - T_s = 2\eta^2 \frac{E}{1-\nu} \frac{x_c(1-x_c)}{nk_B} \approx 80 \text{ K} \tag{9}$$
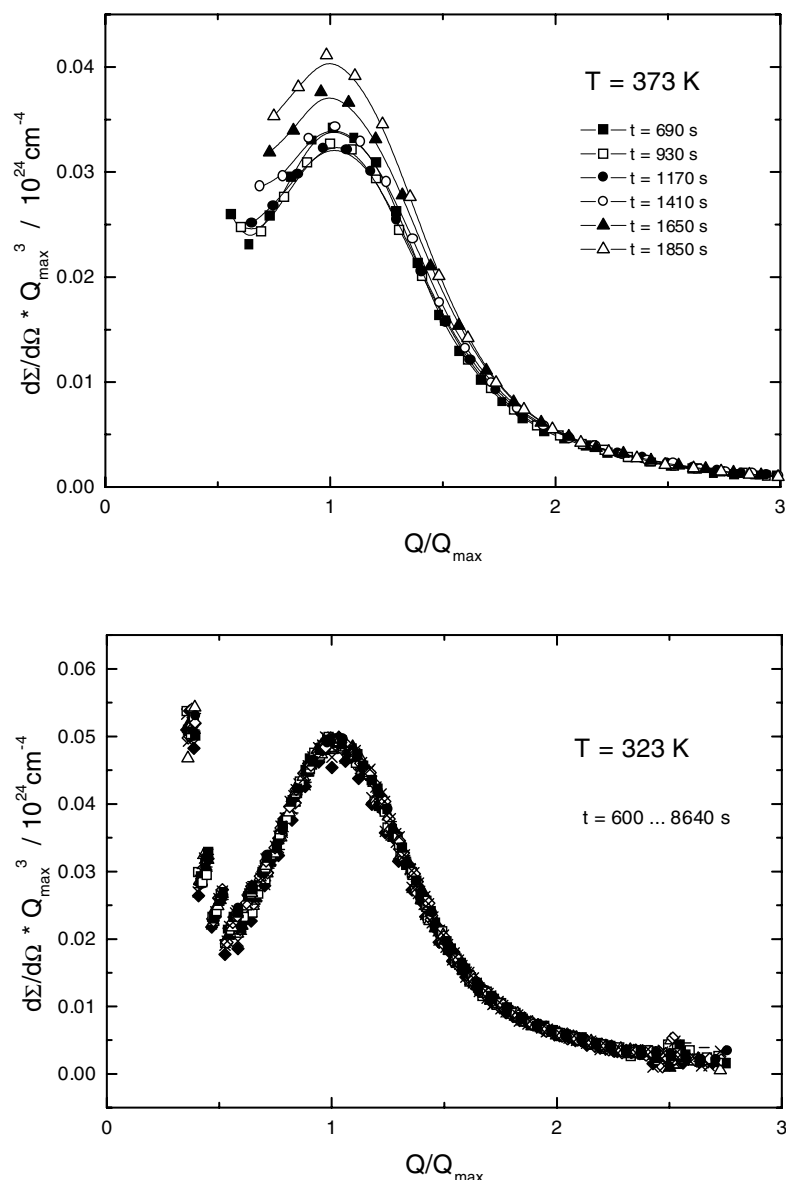
Figure 14. The scaling behaviour of the intensity scattered from $Ag_{0.45}Na_{0.55}Br$ at 373 K (top) and 323 K (bottom).

where η is the relative difference of the lattice parameters of the pure substances ($\Delta a/a \approx 0.034$ [25]), x_c is the critical concentration (0.5), E is the Young modulus (≈ 25.5 GPa, taken as the average of the inverse stiffness constants s_{11} of the pure substances at 473 K [49]), ν is Poisson's ratio (≈ 0.33), n is the particle density (2×10^{22} cm^{-3}) and k_B is Boltzmann's constant. This value is somewhat smaller than the experimental result. A possible reason for this discrepancy is that the above formula has been derived under the assumption that there are no stresses along the direction of the concentration wave. Unlike the case for metallic alloy systems, however, the phase separation in the AgBr–NaBr system occurs within the almost rigid framework of
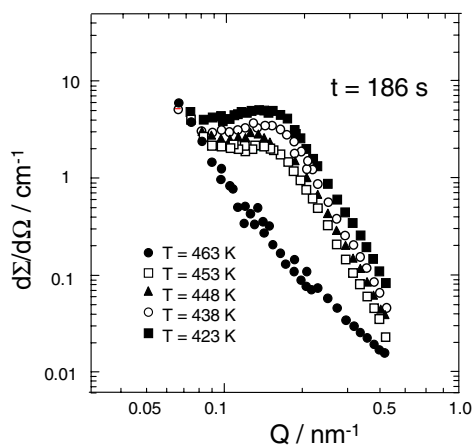
Figure 15. The small-angle intensity profile within the first time step after the quench, for quenches to different temperatures.

the bromine sublattice. Hence, stresses parallel to the modulation can be expected which contribute to the elastic energy of the lattice and lead to a further reduction of the coherent critical point.

4. The mechanism of decomposition

While at temperatures above the spinodal temperature T_s, small-angle scattering and diffraction yield consistent information about the nucleation mechanism of phase separation, the situation changes drastically on cooling below T_s. In this regime, the two different experimental techniques obviously monitor two different aspects of the decomposition process which take place on two different timescales. The SANS directly reflects the chemical demixing via the scattering contrast while the diffraction yields the mechanical relaxation of the underlying bromine lattice.

Hence, we arrive at the following interpretation of the mechanism for phase separation in terms of spinodal decomposition below 460 K.

At very short times, within some 100 s after quenching, concentration fluctuations grow and give rise to the correlation peak in the small-angle scattering. The characteristic length scale is of the order of 20 nm. Simultaneously, the well defined lattice is deformed due to concentration gradients and/or coherency strains since the lattice parameters of the pure compounds differ appreciably. Consequently, the Bragg reflection is broadened almost instantaneously, but its position and the average lattice parameter remain almost unchanged. The structureless intensity distribution covers a Q-range of about $0.7 \, \text{nm}^{-1}$. In particular, there are no indications of satellites which might have been expected at positions in Q-space which are separated from the Bragg peaks by Q_{max} [50, 51].

In the next stage, the morphology of the precipitates changes and the process of Ostwald ripening takes place. The $t^{-1/3}$-law of Lifshitz and Slyozov holds for the time dependence of the correlation wave vector Q_{max} and, hence, the radius of the precipitates. In this period the Bragg profiles do not change appreciably. This finding is a direct proof that the line broadening cannot simply be due to particle size effects. Such effects have in fact been observed by Morii *et al* in the alloy system Mn–Cu [52] where the width of the Bragg reflections decreases appreciably during coarsening. Here, the unchanged continuous intensity distribution indicates

that particle size effects play a minor role and that there are still no well defined lattices of the product phases. The mechanical relaxation of the lattice is hindered by coherency strains.

Only after the grains have reached some critical size larger than 40 nm do they adapt their equilibrium lattice constant and do the coherency strains reduce. Correspondingly, sharp Bragg reflections start to grow from the broad intensity distribution until equilibrium is reached. The onset of this relaxation is reflected by the end of the plateau range of the correlation function $C(t)$ (see figure 9). This last stage takes place on a much larger timescale than the phase separation itself and is extremely temperature dependent. In fact, for temperatures below 400 K this mechanical relaxation could not be observed within the timescale of the present experiment.

Interestingly, the primary demixing process is completed within some 100 s even at low temperatures. Moreover, the characteristic decomposition time seems to be hardly temperature dependent. For a rather long time, the system remains, however, in a metastable state dominated by mechanical strains and characterized by correlation lengths of the order of 20–40 nm.

Additional support for this interpretation stems from the absolute SANS intensities, as detailed below.

For a system of well defined precipitates of concentrations x_1 and x_2 within a matrix of composition x_m, the integrated intensity is given by

$$4\pi \int_0^\infty \frac{d\Sigma}{d\Omega}(Q)Q^2\, dQ = (2\pi)^3 \left\{ (\rho_1 - \bar{\rho})^2 \frac{V_1}{V_{\text{tot}}} + (\rho_2 - \bar{\rho})^2 \frac{V_2}{V_{\text{tot}}} + (\rho_m - \bar{\rho})^2 \frac{V_m}{V_{\text{tot}}} \right\} \tag{10}$$

where the ρ_i are the respective densities of the scattering lengths of the individual phases. If the particle density is not changed by decomposition, mass conservation leads to the well known relation [53]

$$4\pi \int_0^\infty \frac{d\Sigma}{d\Omega}(Q)Q^2\, dQ = (2\pi)^3 (\rho_A - \rho_B)^2 (x_1 - x_m)(x_m - x_2)\alpha \tag{11}$$

where ρ_A and ρ_B are the scattering length densities for the pure compounds A and B, respectively. If the variations of the lattice constants are taken into account, the above formula has to be altered to

$$4\pi \int_0^\infty \frac{d\Sigma}{d\Omega}(Q)Q^2\, dQ = (2\pi)^3 \left\{ \left(\frac{n_1 x_1 - n_m x_m(1 + (\bar{\rho} - \rho_m)/(\alpha\rho_m))}{n_1 x_1 - n_2 x_2} \rho_2^2 \right. \right.$$

$$\left. \left. + \frac{n_m x_m(1 + (\bar{\rho} - \rho_m)/(\alpha\rho_m)) - n_2 x_2}{n_1 x_1 - n_2 x_2} \rho_1^2 - \rho_m^2 \right) \alpha + \rho_m^2 - \bar{\rho}^2 \right\} \tag{12}$$

where the n_i are the particle densities in the individual phases. Obviously, the asymptotic value of the small-angle intensity for complete phase separation ($\alpha \to 1$) can be directly calculated for different temperatures from the phase diagram. The corresponding results are shown in figure 16. The solid line corresponds to the equilibrium state with the appropriate lattice constants of the precipitates according to equation (12). The dashed line represents the intensity expected for a decomposition into a metastable state without mechanical relaxation of the lattice according to equation (11) (constant particle density). For this calculation it is assumed that the final concentrations may be estimated from the equilibrium ones (binodal curve) just by shifting the binodal by $\Delta T_s = 100$ K to lower temperatures to obtain the coherent, metastable miscibility gap. The symbols in figure 16 represent the experimentally determined intensities as obtained just after the steep initial increase (see figure 13). There is a remarkable agreement between experiment and the prediction for decomposition at constant particle density. Moreover, it can be expected that there will be another increase of the SANS intensity by almost a factor of 3 as soon as the lattice relaxes; the sodium-rich phase expands while the silver-rich phase contracts and the stable equilibrium state is approached.
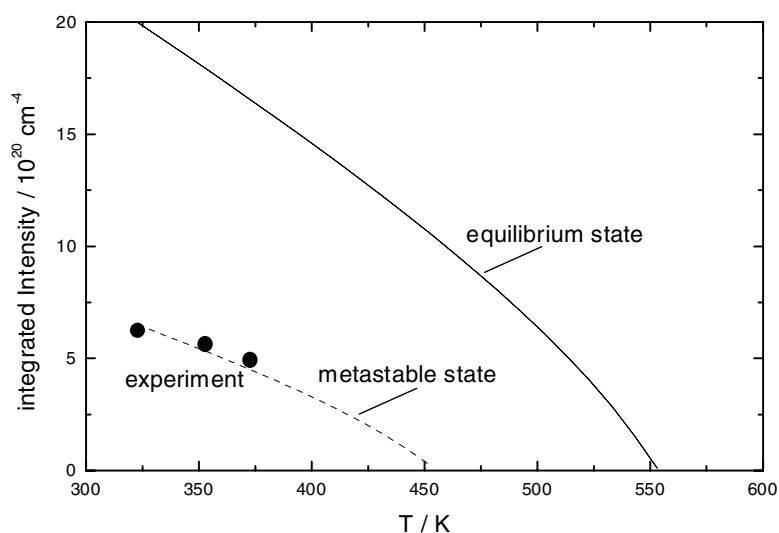
Figure 16. The expected integrated small-angle intensity for complete decomposition into the product phases with relaxed lattice constants (full line). The dashed line corresponds to the decomposition at constant particle density.

Interestingly, a similar two-step behaviour of the integrated SANS intensity has been observed in Ni–Ti alloys by Vyskocil *et al* [54].

Recalling the time dependence of the correlation function $C(t)$ of the Bragg intensity (figure 9), we realize that the mechanical relaxation starts at the end of the plateau, namely after about 300 s at 403 K and after more than 1000 s below 385 K. Comparing with figure 11, we infer that the length scale of the decomposition pattern grows to some 40 nm before the coherency strains are removed by mechanical relaxation and the concentrations approach the stable equilibrium.

In the strained crystal the silver-rich phase exhibits a lattice constant which is larger than in equilibrium. Hence, it behaves as if subjected to a tensile stress. The opposite is true for the sodium-rich phase. From the difference in lattice constants we obtain a rough estimate for the internal stresses: at 373 K, the coherent miscibility gap extends from $x_1 = 0.79$ to $x_2 = 0.22$. The corresponding lattice parameters for the relaxed lattice are obtained via Végard's rule as 0.582 nm and 0.593 nm, respectively, while the lattice parameter of the metastable system is 0.588 nm. Using an average Young modulus $E \approx 30$ GPa, we arrive at a value for the internal stress of about 0.3 GPa.

5. Conclusions

We have shown that the combination of diffraction and small-angle scattering yields detailed information about the demixing process in ionic solids. For the system AgBr–NaBr it is demonstrated that the decomposition is dominated by nucleation and growth as long as the ageing temperature is above $T_s \approx 458$ K. Typical grain sizes are estimated to be several hundred nm. Below T_s, the typical features of spinodal decomposition are observed. We were able to show that coherency strains persist for long times during the coarsening of the decomposition pattern. The mechanical relaxation does not take place before the characteristic length scale becomes of the order of 40 nm. The bromine sublattice thus provides an almost

rigid frame for the phase separation within the cation subsystem. Metastable modulated structures characterized by internal stresses of about 0.3 GPa can be prepared which exist over a long period of time.

Similar experiments on other ionic systems with different lattice parameter mismatch, like AgCl–NaCl or KCl–NaCl, have been performed. The results will be presented in separate publications [55]. Moreover, it has already been demonstrated that, in spite of the large internal strains, the decomposition in the system AgBr–NaBr may be studied even for single crystals [18]. Hence, the direct observation of the evolution of interatomic interactions by means of inelastic neutron scattering from phonons will be possible. Moreover, we believe that Bragg satellites could be observable during spinodal decomposition in single crystals.

Acknowledgments

References

[1] Raghavan V and Cohen M 1975 *Treatise on Solid State Chemistry* vol 5, ed A Hannay (New York: Plenum) p 67
[2] de Fontaine D 1975 *Treatise on Solid State Chemistry* vol 5, ed A Hannay (New York: Plenum) p 129
[3] Gunton J D, San Miguel M and Sahni P S 1983 *Phase Transitions and Critical Phenomena* vol 8, ed C Domb and J L Lebowitz (London: Academic) p 267
[4] Komura S 1988 *Phase Transitions* **12** 3
[5] Binder K 1991 *Materials Science and Technology* vol 5, ed R W Cahn, P Haasen and E J Kramer (Weinheim: VCH) p 405
[6] Kampmann R and Wagner R 1993 *Mater. Sci. Technol.* **9** 215
[7] Hendricks R W, Baro R and Newkirk J B 1964 *Trans Metall. Soc. AIME* **230** 930
[8] Hendricks R W and Borie B S 1967 *Small Angle X-Ray Scattering* ed H Brumberger (New York: Gordon and Breach) p 319
[9] Suslova V N, Shmidova N I, Zavadovskaya E K and Zvinchuk R A 1970 *Sov. Phys.–Dokl.* **15** 500
[10] Wong C K 1971 *MS Thesis* SUNY at Stony Brook, NY
[11] Wolfson R G, Kobes W and Fine M E 1966 *J. Appl. Phys.* **37** 704
[12] Fancher D L and Barsch G R 1971 *J. Phys. Chem. Solids* **32** 1303
[13] Bhardwaj M C and Roy R 1971 *J. Phys. Chem. Solids* **32** 1603
[14] Ahtee M, Inkinen O, Koski H, Pehkonen S and Vikberg P 1970 *Z. Naturf.* a **25** 1732
[15] Jantzen C M F and Herman H 1978 *Phase Diagrams (Materials Science and Technology vol 5)* ed A M Alper (New York: Academic) p 127
[16] Eckold G and Trzeciok D 1992 *Physica* B **180+181** 315
[17] Eckold G 1992 *Jülich Report* JÜL-2675 (ISSN 0366-0885)
[18] Windgasse J, Eckold G and Güthoff F 1997 *Physica* B **234–236** 153
[19] Gerold V and Kostorz G 1978 *J. Appl. Crystallogr.* **11** 376
[20] Kostorz G 1993 *Phys. Scr.* T **49** 636
[21] Eckold G 1990 *Nucl. Instrum. Methods* A **289** 221
[22] Saito M and Tamaki S 1993 *Solid State Ion.* **60** 237
[23] Tsuji T, Fueki K, Mukaibo T, Ohta T and Watanabe T 1970 *J. Solid State Chem.* **2** 563
[24] Trzeciok D 1976 *Thesis* Göttingen University
[25] Trzeciok D and Nölting J 1980 *Z. Phys. Chem., NF* **119** 183
[26] Whittingham M S 1975 *Electrochim. Acta* **20** 575
[27] Bührer W 1975 *Phys. Status Solidi* b **68** 739
[28] Eckold G and Gupta H C 2001 to be published
[29] Tsuji T, Fueki K and Mukaibo T 1969 *Bull. Chem. Soc. Japan* **42** 2193

[30] Sinistri C, Riccardi R, Margheritis C and Tittarelli P 1972 *Z. Naturf.* a **27** 149
[31] Dähnhardt E and Nölting J 1974 *Ber. Bunsenges. Phys. Chem.* **78** 50
[32] Preidel W and Nölting J 1981 *Z. Phys. Chem., NF* **125** 195
[33] Johnson W A and Mehl R F 1939 *Trans. AIME* **135** 416
[34] Avrami M 1939 *J. Chem. Phys.* **7** 1103
[35] Carmesin H O, Heermann D W and Binder K 1986 *Z. Phys.* B **65** 89
[36] Cahn J W and Hilliard J E 1958 *J. Chem. Phys.* **28** 258
[37] Cook H E 1970 *Acta Metall.* **18** 297
[38] Lifshitz I M and Slyozov V V 1961 *J. Phys. Chem. Solids* **19** 35
[39] Furukawa H 1984 *Physica* A **123** 497
[40] Furukawa H 1989 *J. Phys. Soc. Japan* **58** 216
[41] Hoyt J J, Clark B, de Fontaine D, Simon J P and Lyon O 1989 *Acta Metall.* **37** 1597
[42] Binder K and Stauffer D 1974 *Phys. Rev. Lett.* **33** 1006
[43] Binder K, Billotet C and Mirold P 1978 *Z. Phys.* B **30** 183
[44] Furukawa H 1981 *Phys. Rev.* A **23** 1535
[45] Binder K and Heermann D W 1985 *Scaling Phenomena in Disordered Systems* ed R Pynn and A Skjeltrop (New York: Plenum) p 207
[46] Langer J S 1971 *Ann. Phys., NY* **65** 53
[47] Langer J S, Bar-On M and Miller H D 1975 *Phys. Rev.* A **11** 1417
[48] Cahn J W 1961 *Acta Metall.* **9** 795
[49] Every A G and McCurdy A K 1992 *Landolt–Börnstein New Series* Group III, vol 29, ed D F Nelson (Berlin: Springer) pp 76, 77, 240
[50] Cook H E and Hilliard J E 1969 *J. Appl. Phys.* **40** 2190
[51] Philofsky E M and Hilliard J E 1969 *J. Appl. Phys.* **40** 2198
[52] Morii Y, Gaulin B D and Spooner S 1988 *Dynamics of Ordering Processes in Condensed Matter* ed S Komura and F Furukawa (New York: Plenum) p 239
[53] Gerold V 1961 *Phys. Status Solidi* **1** 37
[54] Vyskocil P, Pedersen J S, Kostorz G and Schönfeld B 1997 *Acta Mater.* **45** 3311
[55] Caspary D and Eckold G 2001 to be published